NUMERICAL IMPLEMENTATION OF STREAMING DOWN THE GRADIENT: APPLICATION TO FLUID MODELING OF COSMIC RAYS

PRATEEK SHARMA * AND PHILLIP COLELLA AND DANIEL F. MARTIN †

Abstract.
The equation governing the streaming of a quantity down its gradient superficially looks similar to the simple constant velocity advection equation. In fact, it is the same as an advection equation if there are no local extrema in the computational domain or at the boundary. However, in general when there are local extrema in the computational domain it is a non-trivial nonlinear equation. The standard upwind time evolution with a CFL-limited time step results in spurious oscillations at the grid scale. These oscillations, which originate at the extrema, propagate throughout the computational domain and are undamped even at late times. These oscillations arise because of unphysically large fluxes leaving (entering) the maxima (minima) with the standard CFL-limited explicit methods. Regularization of the equation shows that it is diffusive at the extrema; because of this, an explicit method for the regularized equation with $\Delta t \propto \Delta x^2$ behaves fine. We show that the implicit methods show stable and converging results with $\Delta t \propto \Delta x$; however, surprisingly, even implicit methods are not stable with large enough timesteps. In addition to these subtleties in the numerical implementation, the solutions to the streaming equation are quite novel: non-differentiable solutions emerge from initially smooth profiles; the solutions show transport over large length scales, e.g., in form of tails. The fluid model for cosmic rays interacting with a thermal plasma (valid at space scales much larger than the cosmic ray Larmor radius) is similar to the equation for streaming of a quantity down its gradient, so our method will find applications in fluid modeling of cosmic rays.

Key words. implicit methods, finite differencing, monotonicity

1. Introduction. Cosmic rays (energetic particles moving close to the speed of light) are an important dynamic and energetic component of our Galaxy. The average cosmic ray pressure in our Galaxy is comparable to the kinetic, thermal, and magnetic pressures [4]. It is important to study the interaction of cosmic rays with the thermal plasma to understand the dynamics and the energy balance in our Galaxy and in other astrophysical objects, e.g., clusters of galaxies.

Cosmic rays are collisionless, with the Coulomb collision time $\gg$ the dynamical timescales. However, cosmic rays do not just leave the system at the speed of light. Cosmic rays are effectively coupled to the thermal plasma by self-generated Alfvén waves that scatter them (e.g., [6]; efficient scattering occurs only when the cosmic rays have a sufficiently large number density; this is usually the case for the majority of cosmic ray particles in the Galaxy; e.g., [16]). These waves are generated by a fast, self-generated instability that arises when the cosmic ray streaming velocity (velocity of the cosmic ray fluid relative to the thermal plasma) exceeds the local Alfvén speed. As a result of this instability, the cosmic ray fluid streams at the local Alfvén speed (down the cosmic ray pressure gradient) with respect to the thermal plasma. Other mechanisms, like MHD turbulence (e.g., [17]) and non-resonant instabilities (e.g., [3]) can also scatter cosmic rays but the qualitative picture of streaming relative to the thermal plasma should hold even in these cases. For simplicity, we focus on the self-generated streaming instability and assume that the cosmic ray fluid streams relative to the thermal plasma at the local Alfvén speed.

*Chandra Fellow, Theoretical Astrophysics Center and Astronomy Department, University of California, Berkeley, CA 94720 (psharma@astro.berkeley.edu).

†Applied Numerical Algorithms Group, Lawrence Berkeley National Laboratory, Berkeley, CA 94720

Although a fully kinetic description is necessary to study the excitation of Alfvén waves (at the cosmic ray Larmor radius scale) and their damping on the thermal plasma, a fluid description, where the cosmic ray fluid streams at the local Alfvén speed relative to the thermal plasma, suffices at scales much larger than the cosmic ray Larmor radius (e.g., the typical cosmic ray Larmor radius is $\ll$ the thickness of our Galaxy, and hence a fluid model of cosmic rays is sufficient to study the large scale dynamics and energetics). The equation governing the cosmic ray pressure is (generalization of 1-D equations from [10])

$$\frac{\partial p_c}{\partial t} + \vec{\nabla} \cdot (p_c \vec{u}) + \vec{\nabla} \cdot (\frac{4}{3} p_c \vec{v}_s) = -p_c \frac{\vec{\nabla} \cdot \vec{u}}{3} - \frac{|\vec{v}_s \cdot \vec{\nabla} p_c|}{3}, \tag{1.1}$$

where p_c is the cosmic ray pressure and $\vec{u}$ is the thermal plasma velocity. The streaming velocity $\vec{v}_s = -\mathrm{sgn}(\vec{B} \cdot \vec{\nabla} p_c) \vec{B} / \sqrt{4\pi\rho}$, where $\vec{B}$ is the magnetic field vector and ρ is the plasma density, is equal to the Alfvén velocity, but down the cosmic ray pressure gradient. Equation (1.1) can be derived by replacing $\vec{u}$ by $\vec{u} + \vec{v}_s$ in the standard internal energy equation for a $\gamma = 4/3$ (relativistic) fluid. The last term on the right hand side of Eq. (1.1) is a loss term since cosmic rays work in pushing the thermal plasma as they stream down their own pressure gradient; there is a compensating heating term in the plasma internal energy equation. This irreversible heating can be understood in the kinetic framework: cosmic ray fluid streaming at speeds slightly larger than the local Alfvén speed results in (usually small amplitude) Alfvén waves at the cosmic ray Larmor radius scale. These waves efficiently scatter the cosmic ray particles. In addition to elastic scattering, cosmic rays also lose their energy to Alfvén wave packets because the self-generated waves are moving, on average (in the fluid sense), away from the cosmic ray particles (this process is the inverse of Fermi acceleration). Thus, a part of cosmic ray energy is converted into Alfvén waves which, in a steady state, damp on the thermal plasma. In fluid modeling (valid at large time and space scales), it is assumed that the cosmic rays directly lose their energy to the thermal plasma via the last term in Eq. (1.1).

Eq. (1.1) can be solved by operator splitting, where each term is updated individually. The terms involving $\vec{u}$ are the usual hyperbolic terms and can be treated with the standard methods. The last term on the right hand side can be implemented such that it is an exact exchange term between the plasma and cosmic ray internal energy equations; this term will probably need to be upwinded. The streaming term (third term on the left hand side) is the main subject of this paper, and will be examined using the following conservative one-dimensional model equation describing streaming down the gradient:

$$\frac{\partial f}{\partial t} + \frac{\partial}{\partial x}(vf) = 0, \tag{1.2}$$

where $f(x,t)$ is a function of space and time, $v = -\mathrm{sgn}(\partial f / \partial x)$, and $\mathrm{sgn}(s) = 1$ if $s > 0$, 0 if $s = 0$, and -1 if $s < 0$. The streaming equation is very similar in appearance to the simple advection equation (but very different in nature as we shall see), but differs from a variable-coefficient advection equation as the advection speed (v) depends, not on x, but on the gradient of f. From here on we focus on the simpler Eq. (1.2) and effective numerical methods to solve it. Once numerical methods for solving Eq. (1.2) are available, the streaming part of Eq. (1.1) can be implemented in an analogous fashion.

Integrating Eq. (1.2) in space (from -$\Delta x/2$ to $\Delta x/2$) and time (from $-\Delta t/2$ to $\Delta t/2$) one obtains,

$$\Delta x \left[f_{0,0^+} - f_{0,0^-}\right] + \Delta t \left[-f\mathrm{sgn}(\partial f/\partial x)|_{0^+,0} + f\mathrm{sgn}(\partial f/\partial x)|_{0^-,0}\right] = 0. \quad (1.3)$$

Evaluating Eq. (1.3) at a maximum of f (similar argument applies at a minimum), one obtains

$$\Delta x \left[f_{0,0^+} - f_{0,0^-}\right] + \Delta t[f_{0^+,0} + f_{0^-,0}] = 0,$$

because the sgn function changes sign across the extremum. Assuming that f is continuous in x, this reduces to

$$\Delta x \left[f_{0,0^+} - f_{0,0^-}\right] + 2\Delta t f_{0,0} = 0.$$

Assuming that f is also continuous in time, this is equivalent to $\Delta x \partial f/\partial t + 2f = 0$. In the limit $\Delta x \rightarrow 0$, this implies $f = 0$, an apparent contradiction. This contradiction also applies to the cosmic ray pressure equation (Eq. 1.1; the last term on the right hand side of Eq. 1.1 reduces to zero on integrating in space at an extremum). A resolution of this apparent contradiction is that, rather than $f = 0$, $\partial f/\partial t \rightarrow -2f/\Delta x$; i.e., f changes infinitely fast at an extremum. A similar behavior is observed for the diffusion equation when applied at a point where f is continuous but the gradient of f changes discontinuously. The analogy with the diffusion equation is deeper; in section 3 we show that the regularized equation is diffusive (and hence parabolic) in nature at extrema. For the diffusion equation the discontinuity in f' is removed instantly and the flux becomes continuous. Similarly, when we regularize the sgn(f') function by $\tanh(f'/\epsilon)$ ($f' \equiv \partial f/\partial x$; see section 3 for the details of regularization that we use), the flux $vf \equiv -f\tanh(f'/\epsilon)$ instantly becomes continuous (see Fig. 4.5 for the plots of vf at different times) at the extrema and $\partial f/\partial t$ is well behaved, just as it is for the diffusion equation. It is reassuring that a unique solution is obtained for the regularized equation (Eq. 3.1) in the limit $\Delta x \rightarrow 0$ and $\epsilon \rightarrow 0$, for a sufficiently small timestep Δt. In Section 5 we show that a unique solution is obtained using other regularizations.

The methods for treating the standard hydrodynamic and magnetohydrodynamic (MHD) equations are quite mature by now, but entirely unexpected numerical problems arise when new physics (as in Eq. 1.1) is added. Thus, the numerical implementation of these new terms must be tested rigorously. For example, simple centered finite differencing of anisotropic thermal conduction can give rise to negative temperatures for large temperature gradients, an unphysical result ([13]). Similarly, here we show that a naive implementation of Eq. (1.2) results in unphysical oscillations.

The paper is organized as follows. Section (2) shows that a standard explicit implementation of Eq. (1.2) results in spurious oscillations of large amplitude. It is shown that a much smaller timestep with $\Delta t \propto \Delta x^3$ can remove oscillations and results in a physically consistent evolution. In section (3) we regularize Eq. (1.2) and develop implicit methods based on it. Section (4) presents test problems (with both continuous and discontinuous initial profiles) which show that physically consistent solutions are obtained using implicit methods with a sufficiently small timestep $\Delta t \propto \Delta x$. In Section (5) we present two different regularizations and show that the same solution is obtained in the converged limit. In section (6) we discuss the nature of the solutions, and conclude with the implications of our methods for the fluid modeling of cosmic rays and for thermal conduction in the collisionless regime.

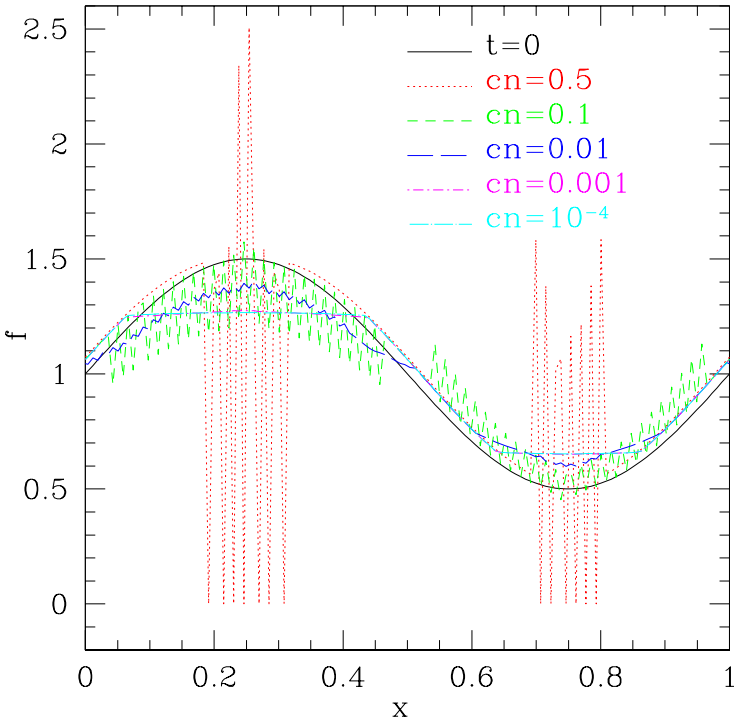

FIG. 2.1. *Profiles at $t = 0$ (solid black line) and $t = 0.02$ for the sine wave initial condition (Eq. 2.1) with different CFL numbers. Number of grid points is 128. Periodic boundary conditions are used. The profiles with cn=0.001 and cn=10^{-4} almost overlap.*

2. Non-monotonicity with explicit schemes using the standard CFL time-step. The standard methods for solving hyperbolic equations fail miserably for solving Eq. (1.2), as demonstrated by a periodic test problem with a smooth initial profile given by

$$f(x, 0) = 1 + 0.5 \sin(2\pi x). \tag{2.1}$$

We show that a standard explicit update scheme with a reasonable Courant-Friedrichs-Lewy (CFL) number ($\Delta t = \mathrm{cn}\Delta x/|v|$, where cn is the CFL number, $|v| = 1$ for Eq. 1.2) gives rise to spurious oscillations even for a smooth initial condition like Eq. (2.1). Figure (2.1) shows the initial profile and profiles at $t = 0.02$ for runs with different CFL numbers; the number of grid points is 128. Eq. (1.2) is evolved using an upwind method with a van Leer slope limiter (e.g., see [8]); such oscillations occur for all explicit methods. As mentioned in the introduction, the streaming equation (Eq. 1.2) is mathematically well-behaved only when the discontinuous $\mathrm{sgn}(f')$ function is replaced by its smoothened form $\tanh(f'/\epsilon)$; thus we use this smoothened form with $\epsilon = 0.1$ to calculate the fluxes. If we use the sgn function instead of the smoothened form, grid scale oscillations in f arise even for an arbitrarily small Δt (oscillation amplitude becomes smaller with a smaller Δt though). The profile with cn=0.5 shows large amplitude oscillations originating from the initial extrema. Although the amplitude of oscillations with cn=0.1 is smaller, the oscillations are more spread out; this

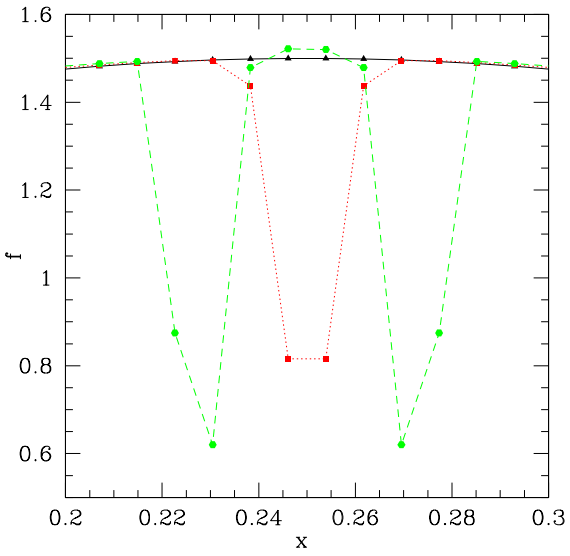

FIG. 2.2. *Zoom in on the profiles at first two timesteps for cn=0.5 in Figure (2.1): the initial profile is marked by a solid line and triangles; the profile at the first timestep by dotted line and squares; and the profile at the second timestep by dashed line and circles. Grid-scale oscillations originate at the local extrema and propagate throughout the box with time.*

is because the number of timesteps to reach $t = 0.02$ is larger with a smaller CFL number (hence spreading out the oscillations). As the CFL number is reduced further the profiles converge to a reasonable-looking f. Profiles with cn=0.001 show small amplitude oscillations, but the profile with cn=10^{-4} does not.

These oscillations originate from the local extrema. With a large timestep (even a CFL-limited timestep is large for the extrema), the fluxes (on both sides) leaving the initial maximum are big enough to reduce the initial maximum way below its initial value (see Fig. 2.2), thus giving rise to an unphysical dip at the location of the initial maximum. Since the dip is a local minimum now, there are large fluxes entering those grid points in the next timestep, again making them a local maximum and simultaneously making the adjoining grid cells a minimum. Now two new local minima are created in cells adjoining the initial maximum, in addition to the initial maximum. In this way oscillations propagate away from the initial extremum as the solution is advanced, resulting in oscillations which spread over the whole domain with time.

One can obtain a limit on the timestep such that new local extrema are not created. Consider a maximum (at f_0) shown schematically in Figure (2.3); we consider the extrema because the oscillations originate there. Considering a piecewise constant reconstruction, let us apply an upwind update of Eq. (1.2) for a single timestep, such that, $f_0^{n+1} = f_0^n - 2\Delta t/\Delta x f_0^n$, $f_1^{n+1} = f_1^n + \Delta t/\Delta x(f_0^n - f_1^n)$. Now imposing monotonicity after a single timestep, i.e., $f_0^{n+1} \geq f_1^{n+1}$ gives,

$$\Delta t \leq |f''|\Delta x^3/(4|v|f), \tag{2.2}$$

since $f_0^n - f_1^n \approx |f''|\Delta x^2/2$ and $f_0^n \gg |f''|\Delta x^2$, where f'' ($\equiv \partial^2 f/\partial x^2$) is evaluated at the extremum. Notice that the timestep restriction will be worse if even higher order

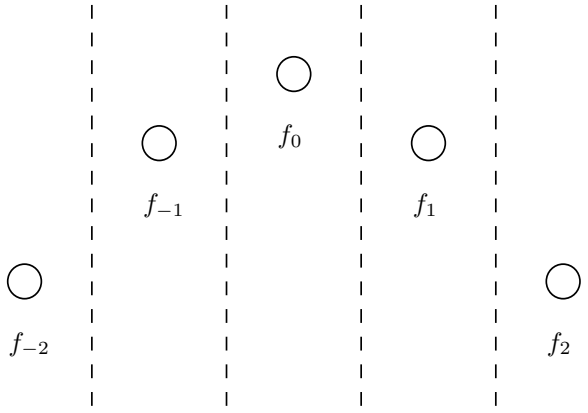

FIG. 2.3. *A schematic representation of a maximum at f_0. Unphysically large fluxes leaving f_0 with the standard CFL-limited timestep result in oscillations seen in Figs. (2.1) and (2.2).*

derivatives vanish, and also that $|f''|$ decreases as the initial profile smoothens with time. A similar condition for monotonicity is obtained at a minimum. Although we have considered an upwind method above, a similar timestep constraint is obtained for any explicit method. A result similar to Eq. (2.2) is obtained by analyzing the regularized form of Eq. (1.2) in section (3). The value of $|f''|$ at extrema for the initial profile in Eq. (2.1) is $2\pi^2$ and the limit on timestep given by Eq. (2.2) is $\Delta t \leq (\pi^2 \Delta x^2/3)\Delta x$, which on using $\Delta x = 1/128$ gives $\Delta t \leq 2 \times 10^{-4}\Delta x$. This is consistent with oscillations seen in Figure (2.1) for cn≥ 0.001 and not for cn$=10^{-4}$.

3. Regularization. Since the advection velocity v can change discontinuously at extrema, the differential form in Eq. (1.2) is well posed only in its regularized form. A similar situation occurs for the Euler/Burger's equations in the absence of viscosity. Motivated by the use of explicit viscosity to make Euler/Burger's equations well-posed, we introduce a physically motivated regularization of Eq. (1.2). A straightforward regularization is obtained by replacing $\mathrm{sgn}(f')$ in Eq. (1.2) by its smooth approximation $\tanh(f'/\epsilon)$, where ϵ is a small parameter.

Thus the regularized form of Eq. (1.2) becomes,

$$\frac{\partial f}{\partial t} - \frac{\partial}{\partial x}\left[f \tanh(f'/\epsilon)\right] = 0, \qquad \text{or} \tag{3.1}$$

$$\frac{\partial f}{\partial t} - \tanh(f'/\epsilon)\frac{\partial f}{\partial x} = \frac{f}{\epsilon}\mathrm{sech}^2(f'/\epsilon)\frac{\partial^2 f}{\partial x^2}, \tag{3.2}$$

where we have used $d\tanh(s) = \mathrm{sech}^2(s)ds$. While the second term on the left hand side of Eq. (3.2) is an advective term, the term on the right hand side of Eq. (3.2) is a diffusive term, which at an extremum (where $f' = 0$) is ff''/ϵ, a diffusive term with the diffusion coefficient f/ϵ. There is a physical justification for such a regularization. As mentioned before, away from the cosmic ray pressure extrema, cosmic ray fluid streams down its pressure gradient along magnetic field lines; in addition to this streaming there is also diffusion (due to pitch angle scattering by the self-excited Alfvén waves, which is typically small, but should be added on the right hand side of Eq. [1.1]) along magnetic field lines. At cosmic ray pressure extrema, the cosmic ray particles have an equal probability to move in either direction (along magnetic field

lines) at the speed of light. However, they are scattered after traveling a distance of the order of the Larmor radius, thus resulting in a diffusive behavior at extrema. Just as viscosity can be ignored at all locations except close to shocks for Euler/Burger's equations, the diffusive behavior of Eq. (3.2) is only effective at extrema.

The time step limit for the stability of the diffusive term in Eq. (3.2) treated explicitly is

$$\Delta t \leq \Delta x^2 \epsilon / 2f; \tag{3.3}$$

on taking $\epsilon \sim f\Delta x/L^2$ (L is the box-size), this scales in the same way as Eq. (2.2). Although this restriction on timestep follows from the linear stability analysis of the discretized diffusion equation, explicit methods with larger timesteps do not blow up because the large diffusion is only concentrated in an infinitesimally small region where $f'' \approx 0$. Away from extrema, the term on the left hand side is like advection. Eq. (3.2) clearly shows that Eq. (1.2) is not hyperbolic, and because of that the methods for hyperbolic equations do not work for this. Since the regularized form in Eq. (3.1) is more transparent and has a less restrictive timestep requirement, we will work with it for testing different explicit and implicit methods. We only focus on conservative schemes because the underlying equation (Eq. 1.2) is conservative.

3.1. Explicit methods. Explicit methods are not as attractive as implicit methods for this problem because of the restrictive timestep (Eq. [3.3]) for stability, but we discuss them for completeness. With the standard CFL timestep, both the Lax-Wendroff and upwind methods give very similar large amplitude oscillations, even with a smooth initial profile (see Fig. [2.1]). With a smaller timestep scaling like Δx^2 (for a fixed ϵ) both methods give physically consistent results.

3.1.1. Lax-Wendroff method. The second order accurate Lax-Wendroff discretization ([7]) for Eq. (3.1) is obtained by observing that

$$f(x, t+\Delta t) = f(x,t) + \Delta t \frac{\partial f}{\partial t} + \frac{\Delta t^2}{2}\frac{\partial^2 f}{\partial t^2},$$

where partial derivatives ($\dot{f} \equiv \partial f/\partial t$) are evaluated at (x,t). Using, $\dot{f} = [f \tanh(f'/\epsilon)]'$ (Eq. [3.1]), $\ddot{f} = [\partial(f\tanh(f'/\epsilon))/\partial t]'$, and expanding the time derivatives in terms of space derivatives, one gets,

$$\frac{f_i^{n+1} - f_i^n}{\Delta t} = \frac{\partial}{\partial x}\left\{ f\tanh(f'/\epsilon) + \frac{\Delta t}{2}\left[\tanh(f'/\epsilon)[f\tanh(f'/\epsilon)]' + \frac{f}{\epsilon}\mathrm{sech}^2(f'/\epsilon)[f\tanh(f'/\epsilon)]''\right]\right\}, \tag{3.4}$$

where quantities on the right hand side are simply averaged to be centered at (i,n). The above discretization is clearly conservative.

3.1.2. Upwind method. The explicit upwind discretization of Eq. (3.1) is given by

$$f_i^{n+1} = f_i^n - \frac{\Delta t}{\Delta x}\left(F_{i+1/2}^{n+1/2} - F_{i-1/2}^{n+1/2}\right), \tag{3.5}$$

where the flux ($F_{i+1/2}^{n+1/2}$) is calculated in an upwind fashion using a standard first order slope limiter (we are using the van Leer limiter; [15, 8]). The flux equals

$$F_{i+1/2}^{n+1/2} = \begin{cases} v\left(f_i^n + \sigma_i \frac{[\Delta x - v\Delta t]}{2}\right), & \text{for } v > 0, \\ v\left(f_{i+1}^n - \sigma_{i+1}\frac{[\Delta x + v\Delta t]}{2}\right), & \text{for } v \leq 0, \end{cases} \tag{3.6}$$

where $v = -\tanh(f'/\epsilon)^n_{i+1/2}$, $\sigma_i = L[f'_{i+1/2}, f'_{i-1/2}]$ (L is a slope limiter like van Leer's).

3.2. Implicit methods. Implicit methods are attractive because longer timesteps, scaling as Δx and not as Δx^2, can be used to give stable and converging results as the resolution is increased.

3.2.1. Linearized implicit method. Assuming smoothness of f', we can write the backward-Euler expansion of $\tanh(f'/\epsilon)$ evaluated at timestep $(n+1)$ in Eq. (3.1) as

$$\tanh(f'/\epsilon)^{n+1} = \tanh(f'/\epsilon)^n + \frac{1}{\epsilon}\mathrm{sech}^2(f'/\epsilon)^n \left(f'^{,n+1} - f'^{,n}\right). \tag{3.7}$$

In writing above we have linearized the implicit approximation in $f'^{,n+1}$. The linearized (semi-)implicit flux for the discretized equation (centered in space), using above, can be written as

$$\begin{aligned} F^{n+1}_{i+1/2} = -\Big(& f^{n+1}_{i+1}\left[\frac{1}{2}\tanh(f'/\epsilon)^n_{i+1/2} + \frac{1}{\epsilon\Delta x}\mathrm{sech}^2(f'/\epsilon)^n_{i+1/2} f^n_i\right] \\ & + f^{n+1}_i\left[\frac{1}{2}\tanh(f'/\epsilon)^n_{i+1/2} - \frac{1}{\epsilon\Delta x}\mathrm{sech}^2(f'/\epsilon)^n_{i+1/2} f^n_{i+1}\right]\Big), \end{aligned} \tag{3.8}$$

which is linear in f^{n+1}. Thus the implicit form of Eq. (3.1), using above, can be evolved using the standard tridiagonal solver (since we are imposing periodic boundary conditions the tridiagonal solver is combined with the Sherman-Morrison formula; e.g., [11]).

3.2.2. Nonlinear implicit method. Instead of linearizing the implicit equation, as we did in the previous section, we can use a fully-implicit nonlinear method. The nonlinear implicit equation can be solved using a Krylov subspace method like the generalized minimal residual method (GMRES; [12]). Eq. (3.1) can be discretized as a nonlinear matrix equation $M(f^{n+1})f^{n+1} = f^n$, where the matrix-vector product to be used in GMRES is given by

$$MV_i = V_i - \frac{\Delta t}{\Delta x}\left\{V_{i+1/2}\tanh(V'/\epsilon)_{i+1/2} - V_{i-1/2}\tanh(V'/\epsilon)_{i-1/2}\right\}. \tag{3.9}$$

The matrix equation is solved iteratively until the relative error is small enough (we choose 10^{-12} as the relative error tolerance). Since matrix M is diagonally dominant, for a sufficiently small Δt, this implicit scheme converges rapidly.

3.2.3. Semi-implicit method. The implicit methods we consider are formally only first order accurate in time, but can be made second order accurate by combining implicit and explicit methods, similar to the Crank-Nicolson scheme for the diffusion equation. The regularized equation (Eq. [3.1]) can be discretized as

$$\begin{aligned} \frac{f^{n+1}_i - f^n_i}{\Delta t} = & \frac{g}{\Delta x}\left[f_{i+1/2}\tanh(f'/\epsilon)_{i+1/2} - f_{i-1/2}\tanh(f'/\epsilon)_{i-1/2}\right]^n \\ & + \frac{(1-g)}{\Delta x}\left[f_{i+1/2}\tanh(f'/\epsilon)_{i+1/2} - f_{i-1/2}\tanh(f'/\epsilon)_{i-1/2}\right]^{n+1}, \end{aligned} \tag{3.10}$$

where the update is split into an explicit and implicit part. We update the explicit piece using the Lax-Wendroff method and the implicit piece using the nonlinear implicit scheme. Results for different test problems are similar as the implicit schemes.

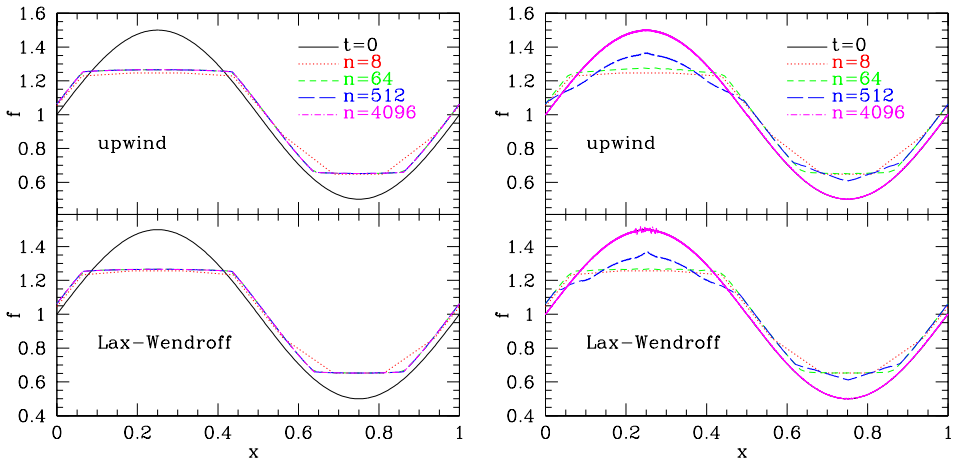

(a) $\Delta t = \epsilon \Delta x^2/3$ (b) $\Delta t = 0.002\Delta x$

FIG. 4.1. *The initial profile (Eq. [2.1]) and profiles at* $t = 0.02$ *using (a)* $\Delta t = \epsilon \Delta x^2/3$ *(*$\epsilon = 0.1$*) and (b)* $\Delta t = 0.002\Delta x$ *for explicit schemes. Results with upwind and Lax-Wendroff methods look similar. Unlike with* $\Delta t \propto \Delta x^2$*, with* $\Delta t \propto \Delta x$ *the results do not converge as the spatial resolution is increased.*

Somewhat surprisingly, the convergence with increasing number of grid points for the semi-implicit ($g = 1/2$ in Eq. [3.10]) scheme is not very different from the fully implicit methods (see Fig. [4.4]). Notice that f' is not continuous (discontinuity occurs where the flattened maxima/minima is connected to the advecting part of the solution; e.g., Figs. [4.1a, 4.2a]) for the streaming sine wave profile so the order of convergence is not easy to establish analytically. Also, the timestep is so small that the temporal error is dominated by the spatial truncation error.

4. Test problems. In this section we compare the different methods from section (3), as they are applied to solve the regularized equation (Eq. [3.1]). We consider two periodic, one-dimensional test problems: an initial sine wave given by Eq. (2.1) and an initial square wave. We use $\epsilon = 0.1$ unless mentioned otherwise.

4.1. Smooth initial profile. Figure (4.1) shows profiles at $t = 0.02$, beginning with the initial profile in Eq. (2.1), for explicit methods using $\Delta t = \epsilon \Delta x^2/3$ Fig (4.1a; consistent with the timestep limit in Eq. [3.3]) and $\Delta t = 0.002\Delta x$ (Fig [4.1b]). While profiles converge to the physically consistent solution with increasing resolution when $\Delta t \propto \Delta x^2$, increasing resolution with $\Delta t \propto \Delta x$ results in unphysical results as the resolution is increased. The convergence of $\Delta t \propto \Delta x^2$ and the non-convergence of $\Delta t \propto \Delta x$ is seen clearly from the plot in Figure (4.3a). While L_1 error decreases for $\Delta t \propto \Delta x^2$, it increases for number of grid points larger than 16 for $\Delta t = 0.002\Delta x$. Non-convergence starts once the timestep is longer than the limit in Eq. (3.3), which happens for $n > 16$ for $\Delta t = 0.002\Delta x$. Although Eq. (3.3) is the stability time limit on the diffusion term in Eq. (3.2), results do not blow up because diffusion $\propto 1/\epsilon$ is only limited to a small length-scale $\propto \epsilon$.

Quite surprisingly, the numerical experiments show that the implicit methods also require a small enough Δt for convergence. This is probably because of the need to accurately resolve diffusion over small length scales ($\propto \epsilon$). With $\epsilon = 0.1$, only for

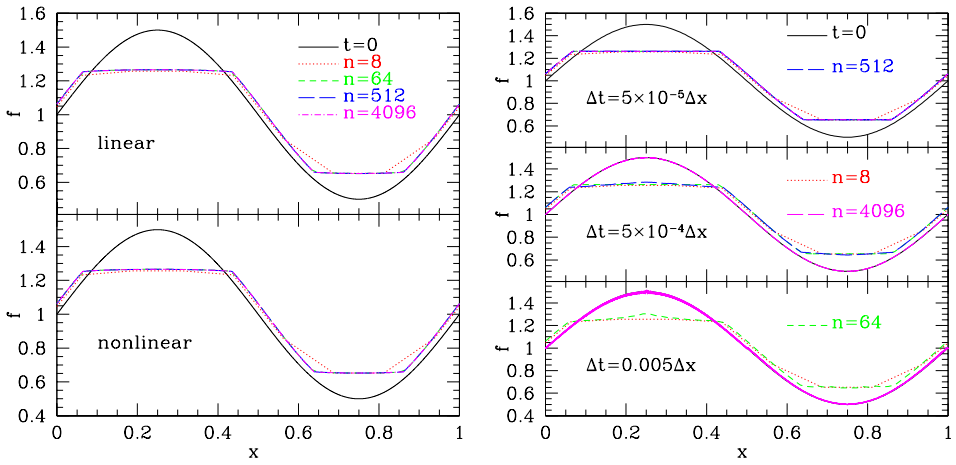

(a) implicit methods, $\epsilon = 0.1$ (b) linearized implicit method, $\epsilon = 0.01$

FIG. 4.2. *The initial profile (Eq. [2.1]) and profiles at* $t = 0.02$ *using* $\Delta t = 0.005\Delta x$ *for (a) implicit schemes with* $\epsilon = 0.1$ *, and (b) the linearized implicit method for* $\epsilon = 0.01$ *and with* $\Delta t = 0.005\Delta x,\ 5 \times 10^{-4}\Delta x,\ 5 \times 10^{-5}\Delta x$. *Results with the linearized implicit method and the nonlinear implicit method look similar. Even for implicit methods, converged results are obtained only when* Δt *is sufficiently small.*

$\Delta t \leq 0.005\Delta x$ do the implicit methods give non-oscillatory convergent results (we have verified this for the number of grid points up to $n = 262144 = 2^{18}$). Figure (4.2a) shows profiles at $t = 0.02$ with implicit methods for the sine wave problem for $\epsilon = 0.1$ and $\Delta t = 0.005\Delta x$. One gets converged results for $\Delta t \propto \Delta x$, unlike with the explicit methods (it is unclear if it holds as $\Delta x \to 0$ or if non-convergence appears for number of grid points more than the maximum we have tried).

Figure (4.2b) shows profiles for $\epsilon = 0.01$ but with three different choices for Δt, using the linearized implicit method (the nonlinear implicit method gives similar results). Using the same Δt that gave converged results for $\epsilon = 0.1$ ($\Delta t = 0.005\Delta x$), one does not get converged results for $n > 16$ (see Fig. [4.3b]). Even using a ten times smaller timestep ($\Delta t = 5\times10^{-4}\Delta x$; naively one would expect the stable timestep limit to scale with ϵ because at extrema, where oscillations originate, $\tanh[f'/\epsilon] \approx f'/\epsilon$) results in non-convergence for $n > 64$ (see Fig. [4.3b]). However, with $\Delta t = 5 \times 10^{-5}\Delta x$ one can see convergence until $n = 4096$ as seen in Figures (4.2b) & (4.3b); we have verified convergence until $n = 32768 = 2^{15}$ for this case. Although the plot in Figure (4.2b) was done with the linearized implicit method, a similar conclusion is reached for the nonlinear implicit method; namely, the nonlinear iterative method converges only if Δt is similar to the value of Δt which gave converged results with the linearized implicit method .

4.1.1. Numerical Convergence. Figures (4.3) & (4.4) show the error (for the solution at $t = 0.2$) for different methods with the initial sine wave test problem (Eq. [2.1]); Figure (4.3a) shows errors with explicit methods (using $\epsilon = 0.1$) for $\Delta t \propto \Delta x^2$ and $\Delta t \propto \Delta x$; Figure (4.3b) shows errors with implicit methods (using $\epsilon = 0.01$) for different Δt scalings; Figure (4.4) shows errors using $\epsilon = 0.1$, with a stable timestep, for all the different methods discussed in this paper. Since the analytic solution is unknown, we show the Richardson errors. The L_1 Richardson error is given by

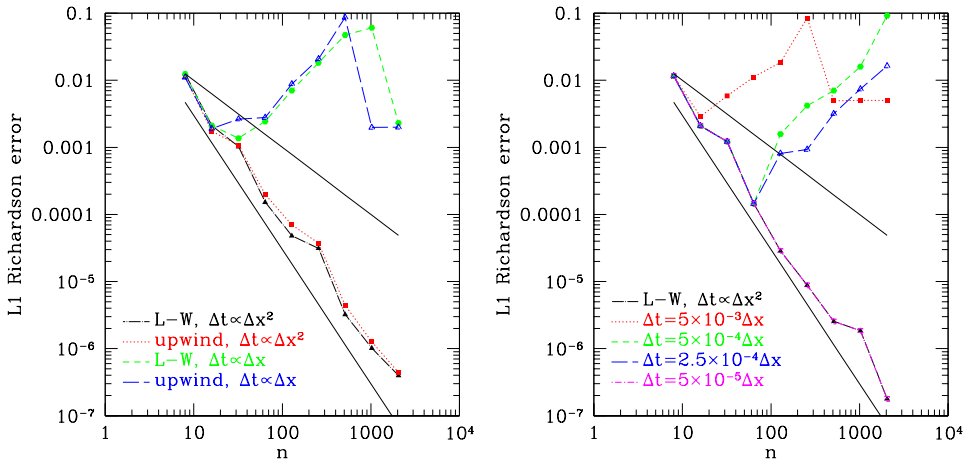

(a) explicit methods with $\epsilon = 0.1$ (b) linearized implicit method with $\epsilon = 0.01$

FIG. 4.3. *L_1 Richardson error (at $t = 0.02$ for the initial profile in Eq. [2.1]) as a function of number of grid points for (a) explicit methods with $\epsilon = 0.1$ (corresponding to Fig. [4.1]) and (b) the linearized implicit with $\epsilon = 0.01$ (corresponding to Fig. [4.2b]) method using different Δt. Timesteps are chosen to be $\Delta t = \epsilon \Delta x^2/3$ and $\Delta t = 0.002\Delta x$ for the explicit methods, and $\Delta t \propto \Delta x$ for the implicit schemes. As seen in Figs. (4.1) and (4.2) converging results are obtained only for a sufficiently small Δt. First- and second-order convergence is indicated by solid lines.*

$\Sigma_{i=1}^{n} |f_i - \overline{f}_i|/n$, where f_i is the numerical solution for f, with n grid points, at the i^{th} grid point, and $\overline{f}_i$ is the interpolation of the solution with $2n$ grid points at the same location. Figure (4.3) clearly shows that only for a sufficiently small Δt do the different (both explicit and implicit) methods converge.

Figure (4.4) shows that the convergence properties of different methods, using a stable timestep, are quite similar; in fact, the errors lie almost on top of each other for upwind, linearized implicit, and fully nonlinear methods. All methods show a close to second-order convergence in the L_1 norm. Somewhat surprisingly the L_1 error at the highest resolution is maximum for the semi-implicit method which, unlike other schemes, is formally second order in time (however, L_2 errors for the semi-implicit method were smaller at the maximum resolution). As noted before, since f' is discontinuous for the solution, a simple order of convergence does not apply.

4.1.2. Nature of the converged solution. Now that we have established that quite small timesteps are required to obtain converged results, even for implicit methods, we will examine the nature of the solutions in more detail. Figure (4.5) shows the time evolution of various quantities (f, $v = -\tanh(f'/\epsilon)$, vf, and f') for $\epsilon = 0.0005$ using the linearized implicit method. Figure (4.5a) shows the converged profile of f at different times for the sine wave test problem (Eq. 2.1), using the linearized implicit method. The extrema of the sine wave are flattened quickly and the $f' \approx 0$ region spreads out in time. The $f' \neq 0$ portion is advected down the gradient at the streaming velocity, as expected. The initial sine wave is fully diffused out in a short time ($t \approx 0.08$). The derivative of the solution changes discontinuously from the flat to steep portions (see Fig. 4.5d).

Fig. (4.6) shows the profiles of various quantities (f, $v = -\tanh(f'/\epsilon)$, vf, and f') at $t = 0.02$ for different ϵs using the linearized implicit method. Timesteps are

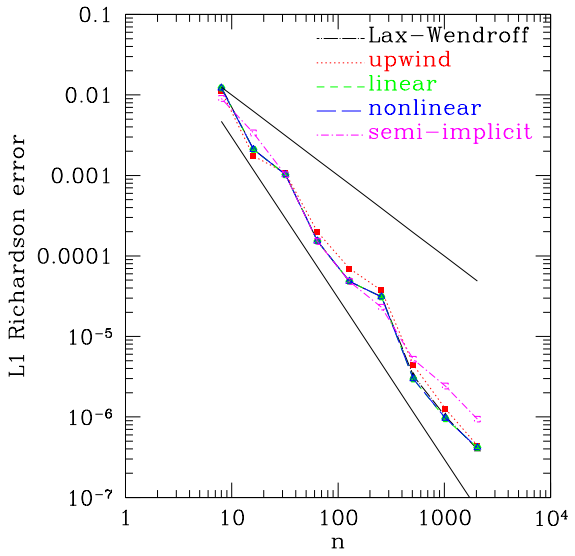

FIG. 4.4. *L_1 Richardson error as a function of number of grid points at $t = 0.02$ with different methods for the initial profile in Eq. (2.1). The errors for Lax-Wendroff, linearized implicit, and nonlinear implicit methods lie almost on top of each other. The solid black lines show scalings as n^{-1} and n^{-2}.*

chosen to be short enough that the solutions are converged for every ϵ. The number of grid point is fixed to be 2048. The profiles of different quantities converge as $\epsilon \to 0$, as required if the regularized equation (Eq. 3.1) is well-posed. Although f' changes discontinuously for the converged profile (in regions where solution transitions from being flat to steep), somewhat surprisingly $v = -\tanh(f'/\epsilon)$ is continuous. As expected, $v = 1$ and is down the gradient, in the steep portions of the solution. In flat portions, v smoothly changes from -1 to 1, crossing 0 where $f' = 0$. Although f' appears to be zero throughout the flat portion of the solution, it is strictly zero only at two points corresponding to the extrema. In flat portion of the solution f' is small (but not 0!) and scales with ϵ. The flux of f due to streaming, vf, is continuous, and is zero only at points where $f' = 0$.

Numerical solution of the regularized equation (Eq. 3.1) is analogous to the numerical solution of the Euler/Burger's equations with explicit viscosity. For these equations the discontinuous profile at the shock is resolved by viscous spreading over a finite scale due to explicit viscosity. Thus, the profiles for various fluid quantities are continuous. Similarly, because of regularized diffusion applied where $f' \approx 0$, various key quantities (f, v, vf shown in Figs. 4.5 and 4.6) become continuous. Similar smoothing of the regularized solution also occurs for an initially discontinuous profile, e.g., the square pulse initial condition discussed in the next section. Fig. (4.4) shows that the solution converges as the resolution is increased for a fixed ϵ. Similarly, Fig. (4.6) shows convergence for a fixed number of grid points as $\epsilon \to 0$. Thus, the solutions of the regularized equation (Eq. 3.1) converge to a unique solution.

4.2. Initial square pulse. In addition to the smooth initial profile, we test different methods with an initial square pulse. Discontinuous cosmic ray pressure profiles can arise in many circumstances, e.g., supernova shocks. The initial profile is

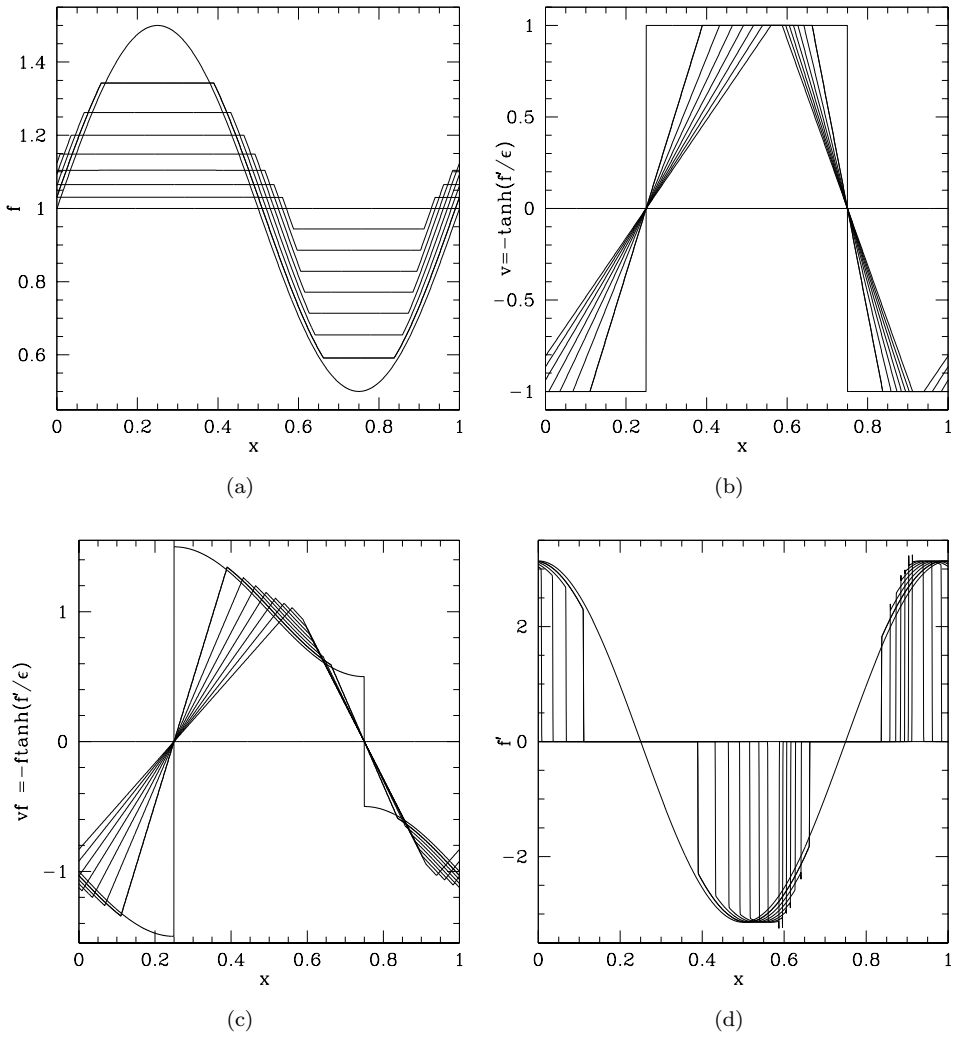

FIG. 4.5. *Various quantities from $t = 0$ until $t = 0.08$ (separated by $\Delta t = 0.01$) as a function of x for the sine wave test problem (Eq. 2.1) using $\epsilon = 0.0005$. The linearized implicit method with the corresponding stable timestep $\Delta t = 5 \times 10^{-7} \Delta x$ is used. The number of grid points is 2048. While f, $v = -\tanh(f'/\epsilon)$, vf are continuous in space, f' is discontinuous where the solution transitions from a flat to a steep profile.*

given by

$$f(x,0) = \begin{cases} 2 & \text{for } 0.4 < x < 0.6, \\ 1 & \text{otherwise.} \end{cases} \tag{4.1}$$

Figure (4.7) shows the solution of Eq. (3.1) using explicit (with $\Delta t = \epsilon \Delta x^2/4$, consistent with Eq. [3.3]; $\epsilon = 0.1$) and implicit (with $\Delta t = 0.005 \Delta x$) methods discussed in section (3) for the square pulse problem (Eq. [4.1]). All methods except the linearized implicit method give converging results with increasing resolution. Unlike with the smooth initial profile, the linearized method fails because it involves taking

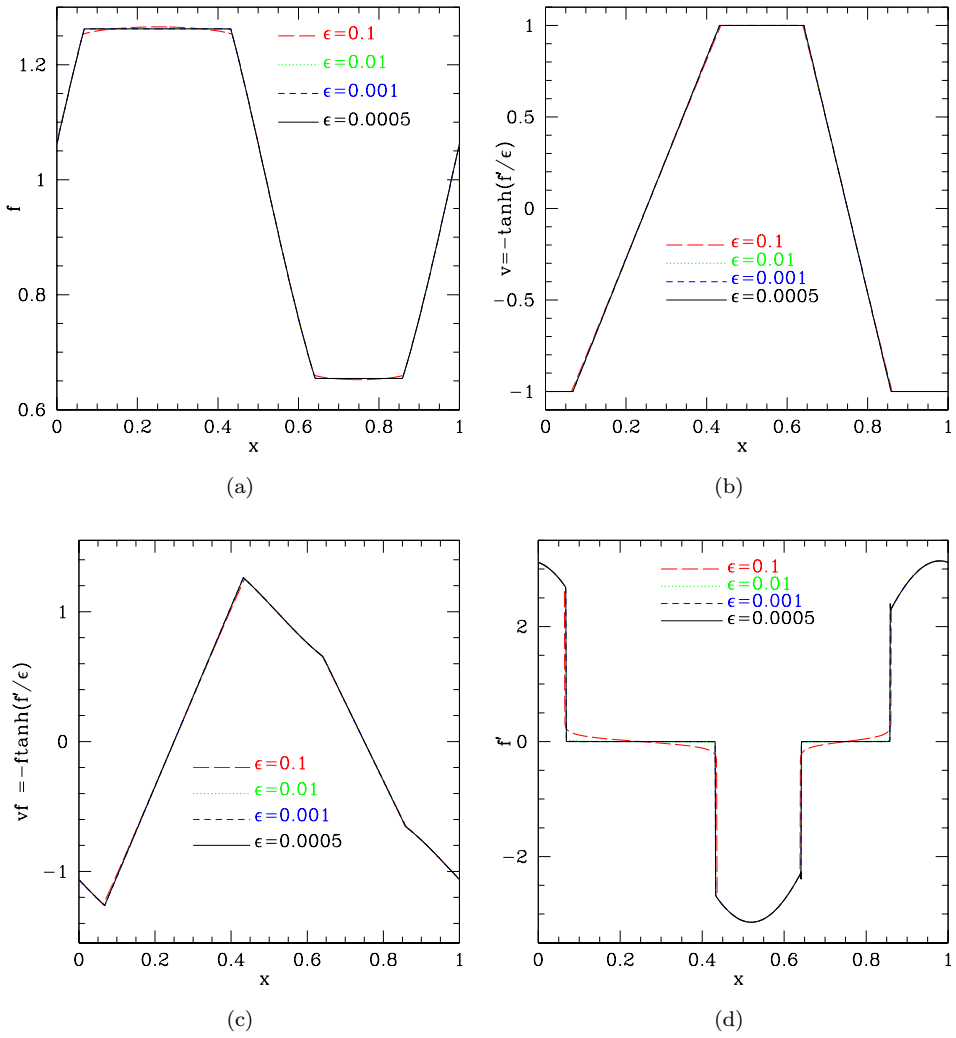

FIG. 4.6. *Various quantities (at $t = 0.02$) as a function of x for the sine wave test problem (Eq. 2.1) using $\epsilon = 0.1$ (blue dashed line), 0.01 (red dotted line), 0.001 (green short-dashed line), & 0.0005 (solid line). The profiles with different ϵs lie almost on top of each other. The linearized implicit method with the corresponding stable timestep ($\Delta t = 5 \times 10^{-3}$, 5×10^{-5}, 5×10^{-7}, $5 \times 10^{-7}\Delta x$ for $\epsilon = 0.1,\ 0.01,\ 0.001,\ 5 \times 10^{-4}$, respectively; identical results are obtained for converged solutions with other methods) is used for different ϵs. The number of grid points is 2048. Converged profiles are obtained as $\epsilon \to 0$.*

the derivative of the discontinuous square wave; the linear expansion about f' used in Eq. (3.7) is not valid when f is discontinuous. This spurious behavior for higher resolutions is eliminated if explicit diffusion (with diffusion coefficient = Δx; recall that the maximum streaming velocity equals unity) is applied. Thus, the linearized implicit method (or a semi-implicit version of it) which can be solved exactly using a fast tridiagonal solver, is a competitive approach even with discontinuous profiles if small explicit diffusion ($\propto \Delta x$) is applied.

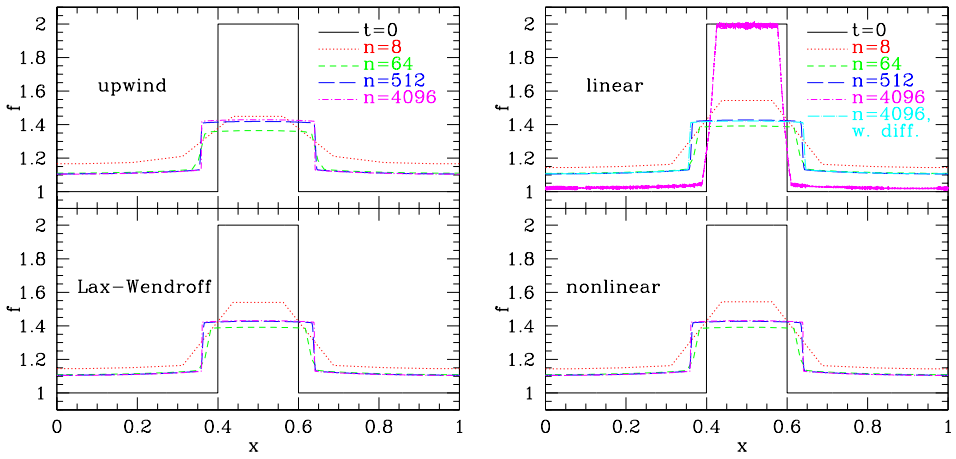

(a) explicit methods (b) implicit methods

FIG. 4.7. *The initial profile (Eq. [4.1]) and profiles at $t = 0.04$ for (a) explicit and (b) implicit methods at different resolutions with $\epsilon = 0.1$. The linearized implicit method gives unphysical results for higher resolutions. However, converged results are obtained if explicit diffusion (with the diffusion coefficient $= \Delta x$) is applied in addition, for the linearized implicit method.*

5. Alternate regularizations. In addition to using the tanh function to approximate the discontinuous sgn function, we also tried two other functions: the error function,

$$\mathrm{erf}(f'/\epsilon) = \frac{2}{\sqrt{\pi}} \int_0^{f'/\epsilon} e^{-t^2} dt, \tag{5.1}$$

and a super-exponential function,

$$\mathrm{Se}(f'/\epsilon) = 2e^{-e^{-f'/\epsilon}} - 1. \tag{5.2}$$

While erf is antisymmetric like the sgn function, Se is not.

Figure (5.1) compares different quantities at $t = 0.02$ using different regularizations and ϵs. The linearized implicit method is used to evolve the regularized streaming equation. Timesteps are chosen such that a converged solution is obtained: for tanh it corresponds to $\Delta t = 5 \times 10^{-3}$, $5 \times 10^{-5} \Delta x$ with $\epsilon = 0.1,\ 0.01$ respectively; for erf, $\Delta t = 2.5 \times 10^{-3}$, $10^{-5} \Delta x$ with $\epsilon = 0.1,\ 0.01$ respectively; and for Se, $\Delta t = 10^{-3}$, $10^{-5} \Delta x$ with $\epsilon = 0.1,\ 0.01$ respectively. Thus, the stable timestep depends on the regularization that is used. Notice that for $\epsilon = 0.1$ the non-antisymmetric regularization with Se results in a profile with is not symmetric with respect to the extrema (see Fig. 5.1a), but the asymmetry is much reduced for $\epsilon = 0.01$. For the regularizations we have tried the result is independent of the regularization in the limit $\epsilon \to 0$, as is desired.

6. Conclusions. We show that the equation governing streaming down the gradient, although appearing deceptively similar to the advection equation (Eq. 1.2), has an entirely different character. It behaves like a diffusion equation at the extrema where $f' \approx 0$ (see Eq. 3.2), and like an advection equation away from extrema. Flux moves from the initial maximum to the initial minimum in the sine wave test problem

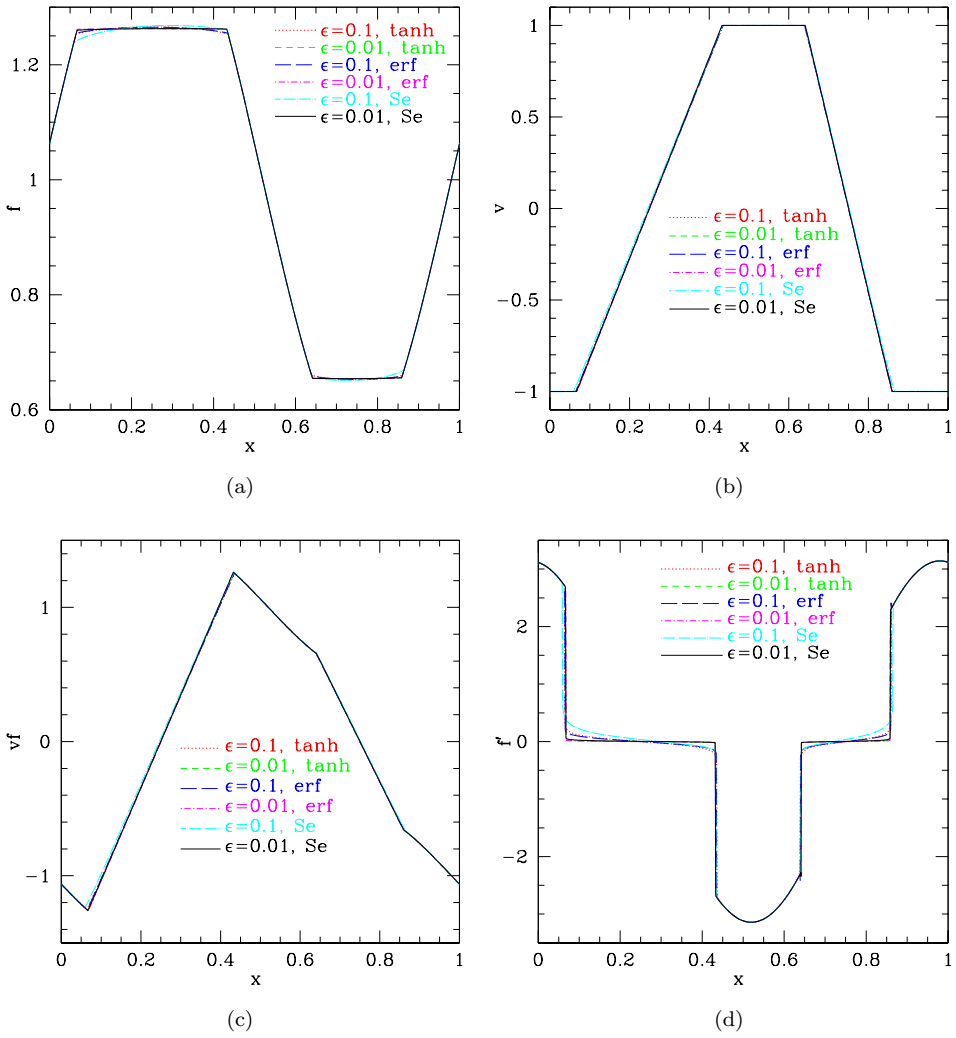

FIG. 5.1. *Various quantities (at $t = 0.02$) as a function of x for the sine wave test problem (Eq. 2.1) using $\epsilon = 0.1$ and 0.01, and with different regularizations. Different quantities become closer to each other as ϵ is reduced. The number of grid points is 2048.*

(initial maximum is reduced and initial minimum is increased) even after a short time (see Fig. [4.5a]) , while the almost flat maximum and minimum are connected by a simple advecting profile. This transport of flux to large distances is a clear sign of the non-hyperbolic nature of Eq. (1.2). Similar signs of large scale transport are seen in the long tails for the square wave problem in Figs. (4.7) and (6.1).

The timestep limit for explicit methods on Eq. (1.2) is severe ($\Delta t \propto \Delta x^3$; see Eq. [2.2]). However, the regularized equation (with a fixed ϵ) is diffusive and the timestep limit for explicit methods scales as $\Delta t \propto \Delta x^2$ (Eq. [3.3]). The most practical are the implicit methods, the timestep limit for which scale as Δx. Although the linearized implicit method gives grid scale oscillations for discontinuous profiles, a small explicit diffusion cures this problem (see Fig. [4.7b]). A fully implicit method using GMRES

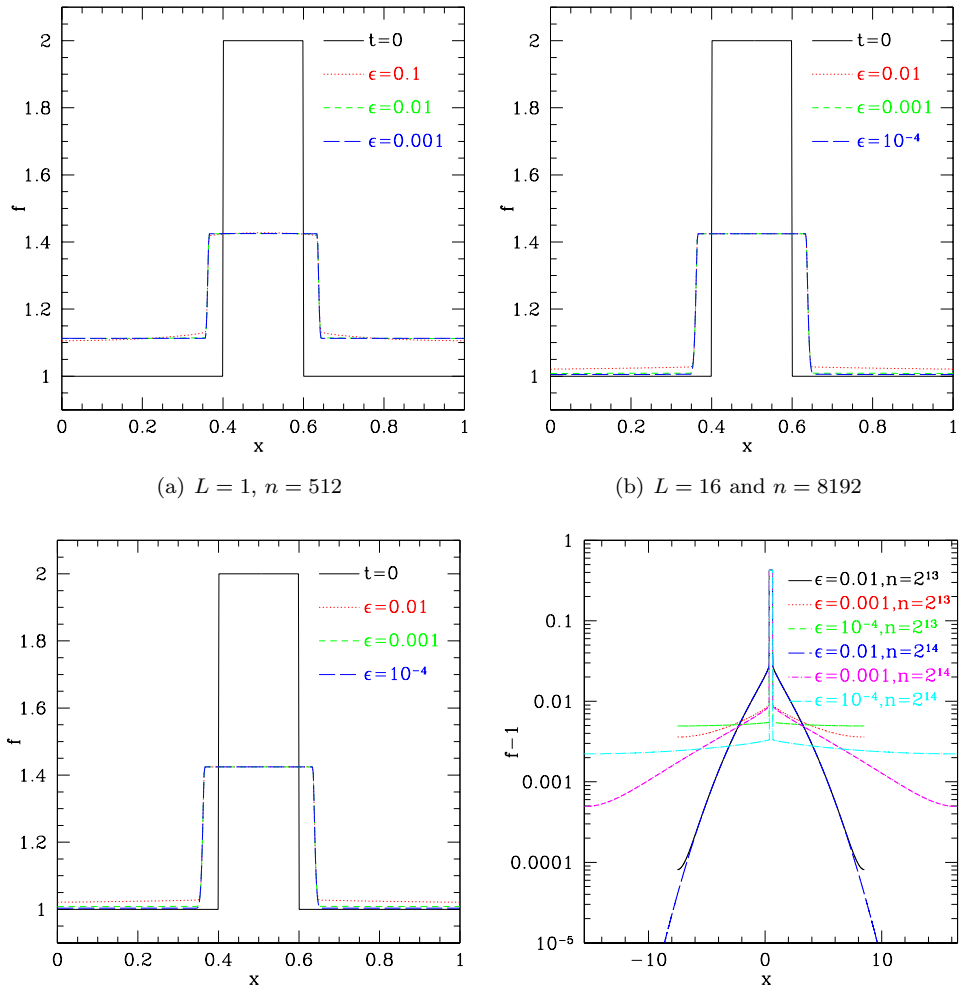

(a) $L = 1$, $n = 512$

(b) $L = 16$ and $n = 8192$

(c) $L = 32$ and $n = 16384$

(d) $f - 1$ *vs.* x

FIG. 6.1. *Profiles at* $t = 0.04$ *for the periodic square wave test problem (Eq. [4.1]; evolved with the Lax-Wendroff method with* $\Delta t = \epsilon \Delta x^2/4$*) for different box sizes (L), number of grid points (n; such that the number of grid points per unit length is the same for all cases) and* ϵ*s:(a) the profiles with* $L = 1$*,* $n = 512$ *are similar for* $\epsilon < 0.1$*; (b) profiles for* $L = 16$ *and* $n = 8192$ *(*2^{13}*); (c) profiles for* $L = 32$ *and* $n = 16384$ *(*2^{14}*); (d) logarithmic plot for* $f - 1$ *as a function of* x *shows that much smaller* ϵ *is required for convergence with a larger box-size.*

does not suffer from such problems and does not require explicit diffusion. Somewhat unexpectedly, the timestep limit for getting converged solutions does not scale linearly with ϵ; a smaller timestep is required for converging results because of an extremely large diffusion (scaling with $1/\epsilon$) at extrema. It is non-trivial to obtain the timestep limit for the convergence of implicit methods (and to establish whether $\Delta t \propto \Delta x$ results in a stable scheme as $\Delta x \to 0$). Traditional linear stability analysis methods (e.g., von Neumann stability analysis) are not useful because the streaming equation is a highly nonlinear equation even in its most basic form (Eq. [1.2]).

Total number of operations with n, the number of grid points in each direction,

scale as: n^{2+d}/ϵ for explicit methods (where d is number of space dimensions); and as n^{1+d}/ϵ for implicit methods, assuming that each implicit update scales as n^d (only if the matrix is well behaved will Krylov methods converge as n^d; however the exact tridiagonal solver will definitely scale as n^d).

Although the analysis of a simple equation like (1.2) is interesting in its own right, the fluid modeling of cosmic rays involves streaming of cosmic rays down their pressure gradient, and is analogous to the simple streaming equation. The generalization to multi-dimensions is straightforward, either in directionally split or unsplit fashion. Unlike with splitting, unsplit methods do not result in a tridiagonal matrix but can be solved by fast Krylov subspace methods. One will need to be careful about calculating $\vec{v}_s$ in the numerical implementation of Eq. (1.1) in multi-dimensions; interpolation of $(\vec{B}\cdot\vec{\nabla})p_c$ using slope limiters (as with anisotropic conduction; e.g., [13]) may be required to preserve monotonicity.

The numerical techniques that we have proposed for solving the streaming equation (Eq. [1.2]) are applicable for different initial (even discontinuous initial profiles can be handled; e.g., Fig. [4.7]) and boundary conditions. Figure (6.1) shows that ϵ required to obtain converged results scales inversely with the box size, as expected (since $f'/\epsilon \sim f/\epsilon L$ must be $\ll 1$ for tanh to be a good approximation of the sgn function). While $\epsilon = 0.1$ is fine to get profiles similar to those obtained by smaller ϵs for $L = 1$, $\epsilon < 0.001$ is required to obtain the $\epsilon \to 0$ solution for $L = 16$ and 32. Notice that the $\epsilon \to 0$ solution consists of a square pulse and extended flat tails. Another important point is that the width of the square pulse and the value of f in the square pulse at $t = 0.04$ is the same for different box sizes and different ϵs. This implies that the flux leaving the square pulse because of advection and diffusion terms in Eq. (3.2) is independent of ϵ, box size, and the boundary condition. If the pulse was just spreading out at a constant velocity (instead of having the extended tails seen in Fig. [6.1]), the value of f at $t = 0.04$ within the square pulse would be $f = 1 + 0.2/(0.2 + 2 \times 0.04) = 1.714$, much larger than the value of 1.425 seen in the converged solutions with streaming. The average rate of decrease for f within the square pulse is almost double for the streaming case with tails as compared to a naive advection solution. Similar large scale transport of flux is seen in the sine wave test problem in Figure (4.5a). The relative proportion of fluxes in the advecting square wave and the long tails depends on the height of the square pulse; higher pulse height leads to a larger flux in the advecting pulse as compared to the extended tails. Thus realizing the diffusive nature of Eq. (1.2) can be astrophysically important, e.g., to accurately obtain the cosmic ray loss rate from the Galaxy and leakage of cosmic rays upstream of supernova shocks.

Comparison of the fluid model (1.1) with particle simulations of cosmic rays is required to test if the cosmic ray streaming model applies for a particular situation (e.g., the tails clearly cannot extend to space scales larger than the light crossing time!) but once the validity of the streaming model for the cosmic ray fluid is established (probably true for Galactic scales), our inferences are applicable. In addition to the implicit diffusive nature of the streaming equation, diffusion of cosmic rays because of scattering by Alfvén waves (ignored in this paper) can result in additional spreading of cosmic rays; the cosmic ray diffusion time is typically much longer than the streaming time for typical Galaxy and galaxy-cluster parameters (e.g., [9]). Streaming of cosmic rays at the local Alfvén speed is extremely important for cosmic ray confinement in the Galaxy for millions of years. Cosmic rays can heat the interstellar and the intracluster medium (due to the $|v_s \cdot \vec{\nabla} p_{\rm cr}|$ term on the right hand side of Eq. [1.1]

or because of convection driven by them) where cosmic ray pressure (compared to the thermal plasma pressure) is significant (e.g., [5, 14]). The often-used equation of saturated thermal conduction, thermal conduction at length scales larger than the electron mean free path, given by (e.g., Eq. 2.8 in [2])

$$\frac{\partial T}{\partial t} = \vec{\nabla} \cdot \left(\hat{b} f_s c_s T \mathrm{sgn}[\hat{b} \cdot \vec{\nabla} T] \right), \tag{6.1}$$

is very similar in nature to the streaming equation (Eq. 1.2). Here T is the plasma temperature, $c_s \propto \sqrt{T}$ is the sound speed, $\hat{b}$ is the magnetic field unit vector, and f_s is a factor of order unity. The presence of sgn function in the heat flux results in a diffusive behavior at extrema. Thus, like the streaming equation, Eq. 6.1 is also parabolic in nature, unlike what earlier analyses which have overlooked the nature at extrema have suggested (e.g., [1]). Thus, the methods developed in this paper will be useful in modeling various astrophysical plasma effects.

Solving the regularized form (Eq. 3.1) of the streaming equation (Eq. 1.2) results in a unique, converged solution, provided that the timestep is small enough. Regularization is analogous to introducing explicit viscosity in solving Euler/Burger's equations and resolving the viscous length scales at the shocks. With regularization the solutions are approximated very accurately, the advection velocity ($v \equiv -\tanh(f'/\epsilon)$) and streaming fluxes ($vf$) are continuous, and converged results are obtained in the limit $\epsilon \to 0$ and $\Delta x \to 0$ (e.g., see Figs. 4.4 & 4.6). In this limit the solutions are also independent of different regularizations we tried (see Fig. 5.1 and §5).

More work is clearly needed to understand the nature (both numerically and analytically) of the streaming equation (Eq. 1.2). For example, like the Euler equations which can result in discontinuous profiles starting with a smooth initial condition, a smooth initial profile for the streaming equation can give rise to discontinuous first derivatives (e.g., f' changes discontinuously from ≈ 0 within the flattened sine wave [e.g., Fig. 4.5] to a constant value outside of it). There is significant transport over large scales (e.g., tails in Fig. [6.1]) because of the parabolic nature of the streaming equation at extrema.

7. Acknowledgements. PS was supported by NASA through Chandra Postdoctoral Fellowship grant number PF8-90054 awarded by the Chandra X-ray Center, which is operated by the Smithsonian Astrophysical Observatory for NASA under contract NAS8-03060. This research was supported in part by the National Science Foundation through TeraGrid resources provided by NCSA and Purdue University. We thank Greg Hammett for providing the GMRES implementation that is used in this paper. PS thanks Eliot Quataert for encouragement, and Xylar Asay-Davis and Ian Parrish for useful discussions. Phil Colella and Dan Martin were supported by the US Department of Energy Office of Advanced Scientific Computing Research under contract number DE-AC02-05CH11231. We thank the anonymous referees for comments which significantly improved the quality of the paper.

REFERENCES

[1] Balbus, S. A., Astrophys. J., 304 (1986) 787
[2] Balsara, D. S., Tilley, D. A., & Howk, J. C., Mon. Not. R. Astron. Soc., 386 (2008) 627
[3] Bell, A. R., Mon. Not. R. Astron. Soc., 353 (2004) 550
[4] Boulares, A. & Cox, D. P., Astrophys. J., 365 (1990) 544
[5] Guo, F. & Oh, S. P., Mon. Not. R. Astron. Soc., 384 (2008) 251
[6] R. M. Kulsrud, Plasma Physics for Astrophysics, Princeton Univ. Press, 2005

[7] Lax, P. & Wendroff, B., Comm. Pure & App. Math. 13 (1960) 217
[8] R. J. Leveque, Finite Volume Methods for Hyperbolic Problems, Cambridge Univ. Press, 2002
[9] Loewenstein, M., Zweibel, E. G., & Begelman, M. C., Astrophys. J., 377 (1991) 392
[10] McKenzie, J. F. & Völk, Astron. & Astrophys., 116 (1982) 191
[11] Press, W. H., Teukolsky, S. A., Vetterling, W. T., & Flannery, B. P., Numerical Recipes in C: The Art of Scientific Computing, Cambridge Univ. Press 1992
[12] Saad, Y. & Schultz, M. H., SIAM J. Sci. Stat. Comput., 7 (1986) 856
[13] Sharma, P. & Hammett, G. W., J. Comp. Phys. 227 (2007) 123
[14] Sharma, P., Chandran, B. D. G., Quataert, E., & Parrish, I. J., Astrophys. J., 699 (2009) 348
[15] van Leer, B., J. Comp. Phys. 23 (1977) 276
[16] Wentzel, D. G., Astrophys. J., 163, 503
[17] Yan, H. & Lazarian, A., Astrophys. J., 614 (2004) 757